A NEW OPERATIONAL MODEL FOR SATELLITE-DERIVED IRRADIANCES
DESCRIPTION AND VALIDATION

Richard Perez[*]

Pierre Ineichen[**]

Kathy Moore[*]

Marek Kmiecik[*]

Cyril Chain[***]

Ray George[****]

Frank Vignola[*****]

[*]   ASRC – The University at Albany, Albany, NY, USA
[**]   CUEPE – University of Geneva, Geneva, Switzerland
[***]   Vaulx-en-Velin, France
[****] NREL, Golden, CO, USA
[*****] University of Oregon, Eugene, OR, USA

ABSTRACT

We present a new simple model capable of exploiting geostationary satellite visible images for the production of site/time specific global and direct irradiances The new model features new clear sky global and direct irradiance functions, a new cloud-index-to-irradiance index function, a new global-to-direct-irradiance conversion model. The model can also exploit operationally available snow cover resource data, while deriving local ground specular reflectance characteristics from the stream of incoming satellite data. Validation against 10 US locations representing a wide range of climatic environments indicates that model performance is systematically improved, compared to current visible-channel-based modeling practice.

1. <u>INTRODUCTION</u>

Geostationary satellites monitor the state of the atmosphere and the earth's cloud cover on a space-and-time continuous basis with a ground resolution approaching 1 km in the visible range. This information can be used to generate time/site specific irradiance data and high-resolution maps of solar radiation. Compared to ground measurements, satellite-derived hourly irradiances have been shown to be the most accurate option beyond 25 km from a ground station (Zelenka et al., 1999). Another noted strength of the satellite resides in its ability to accurately delineate relative differences between neighboring locations, even though absolute accuracy for any given point may not be perfect; hence satellites have proven to be a reliable source of solar microclimate characterization.

Models capable of exploiting satellite observation to generate irradiances range from physically rigorous to purely empirical. At the one end, physical models attempt to explain observed earth's radiances (the brightness seen by the satellite) by solving radiation transfer equations – this requires absolute satellite calibration knowledge and precise information on the composition of the atmosphere. At the other end empirical models may consist of a simple regression between satellite count and a corresponding measurement at the earth's surface. Hybrid models of the type considered here use simple physical modeling approach and some degree of fitting to observations. Extensive reviews and discussion on this subject may be found, e.g., in Schmetz (1989), Noia et al. (1993), Pinker et al. (1995), and Perez, Zelenka et al., (2001).

Simple satellite models derive a cloud index (CI) from the satellite visible channel and use this index to modulate a clear sky global irradiance model that may be adjusted for ground elevation and atmospheric turbidity. In this paper we present an evolution of such a simple satellite model (Zelenka et al., 1999) -- itself based on earlier work by Schmetz (1989) and Cano et al. (1986) -- with the objective of addressing observed remaining weaknesses.

2 <u>OLD MODEL</u>

2.1 <u>Global irradiance (GHI)</u>

This model is an evolution of the original Cano et al. (1986) model, based upon the observation that shortwave (i.e. solar) atmospheric transmissivity is linearly related to the earth's planetary albedo (Schmetz, 1989) sensed by the satellite as earth's radiance and reported as an image-pixel count.

The model includes two distinct parts:

    (1) pixel-to-cloud index (CI) conversion;

    (2) CI to global irradiance conversion.

Pixel-to-cloud index conversion: Image pixels are received as "raw" pixels which are proportional to the earth's radiance sensed by the satellite. A raw pixel is first normalized by the cosine of the solar zenith angle to account for first order solar geometry effect. This normalized pixel is then gauged against the satellite's pixel dynamic range at that location to extract a cloud index (Fig. 1). The dynamic range represents the range of value a normalized pixel can assume at a given location from its lowest (darkest pixel, i.e., clearest conditions) to its highest value (brightest pixel, i.e., cloudiest conditions). The dynamic range at a given location is maintained by the flux of incoming normalized pixels at that location. While the upper bound of the range remains constant (except for a time-line modulation to account for satellite's calibration drift), the lower bound evolves over time as a function of the local ground albedo variations (chiefly snow, moisture, and vegetation effects). Incoming pixels within a sliding time window are used to determine this lowest bound. The old model uses an 18-day window in summer and a shorter 5-day window in winter in an attempt to capture fast evolving snow cover variations. The lower bound is determined as the average of the 10 lowest pixels in the sliding time window. Before being considered for dynamic range maintenance, an incoming pixel is subjected to a secondary normalization to account for a secondary atmospheric air mass effect and for the hot spot effect (Zelenka et al., 1999) .The latter is a function of the sun-satellite angle and incorporates both atmospheric back-scatter brightness intensification and the fact that ground surface becomes brighter as the sun-satellite angle diminishes due to the reduction of ground shadows seen by the satellite (e.g., Pinty and Verstraete, 1991). This secondary normalization is then applied in reverse to the lower bound of the dynamic range before it can be compared to an incoming normalized pixel for the determination of the cloud index as

$$CI = (norpix – low^*) / (up – low^*)$$

where norpix is the cosine-normalized pixel given by:

$$norpix = pix \ am \ soldist,$$

where pix[1] is the "raw" untreated image pixel, where am is the optical airmass and where soldist is the square of the normalized earth-sun distance.

The parameter up is the dynamic range's upper bound and low* is the lower bound after reverse secondary normalization.

Cloud-index-to-GHI Conversion: GHI is determined by:

$$GHI = (0.02 + 0.98 (1 – CI)) Ghc$$

Where Ghc is the clear sky global irradiance per Kasten (Kasten, 1984). Ghc is adjustable for broadband turbidity as quantified by the Linke turbidity coefficient (Kasten, 1980), and ground elevation.

$$Ghc = 0.84 Io cosZ exp \{ -0.027 am [fh1 + (TL-1) fh2] \}$$

With   fh1 = exp(-alt / 8000)
                fh2 = exp(-alt / 1250)

Where Io is the extraterrestrial normal incident irradiance, Z is the solar zenith angle, am is the elevation-corrected air mass, TL is the Linke turbidity coefficient and alt is the ground elevation in meters.

2.2 Direct Irradiance (DNI)

DNI is modeled from the satellite-derived global using the model DIRINT originally developed and validated for ASHRAE (Perez et al., 1992). This model is an evolution of NREL's DISC model, using a "stability index" derived from the consecutive records of GHI input.

2.3 Observed Shortcomings of the Old Model

Model bias: Although overall bias for GHI has generally been found to be acceptable, there remain important seasonal and regional disparities.

Snow cover: The short winter-time sliding window to detect rapid albedo changes caused by snow cover in northern locations leads to diminished model performance, sometime resulting in large winter biases.

---

[1] Depending on its source the value of pix may need additional corrections to reflect the original satellite measurement count. In the US, for instance, data available trough Unidata (2002), a quadratic correction is applied to visible images for better image viewing. This correction should be removed as part of the pixel normalization process.

DNI: DNI is extracted from global using a secondary model that had not been developed to fully account for regional turbidity and ground elevation.

Climate: although the model works relatively well overall in "generic" temperate climates, limitations have been observed in more extreme climates, particularly in very clear arid locations found in the southwestern US, where the models tend to underestimate irradiances (in particular DNI).

3.   NEW MODEL

3.1 Pixel to Cloud Index

The new model features two major evolutions: (1) the utilization of external information for snow cover and (2) an accounting of sun-satellite angle effects individualized for each pixel. A seasonal trend adjustment of the dynamic range's lower bound and a minor modification of the secondary airmass effect normalization are also introduced.

Snow cover: For the USA and parts of Canada, the NOHRSC (2002) maintains a daily report of ground snow cover that is accessible via the Internet. The data are made available on a grid of resolution comparable to our satellite archive. The data may be of three types: (a) no snow cover, (b) snow cover and (c) too cloudy to tell. The satellite model uses this information by resetting the value of the dynamic range's lower bound if a pixel's location switches from no-snow cover to snow cover. This implies dropping the current lower bound and replacing it by the value of new incoming lowest pixels. As these pixels get lower as snow ages and melts, the lower bound naturally regains its snow-free value. This process is illustrated in Fig. 2.

Dynamic range lower bound: Using the external snow cover information frees the model to use a longer time window for the dynamic range in winter. The current model uses a year-round 60-day window which allows a robust determination of the lower bound with many data points. The actual minimum, low, is the average of the forty lowest normalized pixels over this time window. As before the pixels considered for dynamic range maintenance incoming pixels are subjected to a secondary normalization to account for high air mass effects, leading to a fully normalized pixel npix,

$$npix = norpix / (2.283\ h^{-0.26}\ e^{0.004\ h})$$

Where h is the solar elevation in degrees. Further h is set at a minimum value of 1.5^{o} and a maximum value of 65° for solar elevation outside this interval.

This secondary normalization is then applied in reverse, to the dynamic range's lower bound before comparison with incoming cosine-normalized pixels for the determination of the cloud index.

The switch to a longer year-round window was facilitated by introducing a small trend correction ζ, based upon the observed mean seasonal variation of the lower bound (e.g., see the seasonal trend in Fig. 3).

Trend corrected low = ζ low, with ζ = (3 + 0.5 cos(doy π/365) / (3.0 + 0.5 cos((doy-win / 2) π/365))

with: doy = day of year, and win = time window length in days

Sun-satellite angle effects: In the old model we had attempted to account for this effect by using a generic normalization function applicable to all pixels. It soon became apparent that there were strong differences from pixel to pixel, associated with ground cover and soil type. The largest cause of these differences had been overlooked: specular reflectivity of the ground surface. This effect is particularly significant in dry western regions of North America and can vary substantially over short distances. Fig. 3 compares the minimum dynamic ranges traces for Albuquerque, New Mexico, for a morning and a mid-afternoon hour. Using a single lower-bound trace for all points, as in the old model, led to strong mid-afternoon underestimations because naturally brighter afternoon pixels were misinterpreted as having a higher cloud index. This shortcoming was resolved by deriving a unique, different function for each pixel relating each hour's relative minimum to the day's lower bound. Operationally, these individualized pixel functions consist of month-by-hours lookup tables derived from several years of archived satellite data. For a given hour/month this factor, Matfac, is equal to:

   Matfac = low_1 / low,

where low_1 is the dynamic range's lower bound for the considered hour and month, and low is the lower bound for all hours for the considered month. The factor Matfac is used as a multiplicator to the dynamic range's lower bound before comparison with incoming pixels for the determination of the cloud index.

3.2 GHI Generation

As in the old model cloud indices are used to modulate a clear sky global irradiance model that may be adjusted for both broadband turbidity and ground elevation. However, several modifications have been introduced.

Broadband turbidity: Ineichen and Perez (2002) recently proposed a revised formulation of the Linke Turbidity coefficient to remove its dependence on solar geometry. This new formulation was used to generate a seasonal grid of TL for the North American continent, based upon gridded climatological aerosol, ozone and water vapor data that had previously been assembled for the preparation of the NSRDB (1995). The new formulation could also be used, as appropriate, to generate TL "on the fly" from regional ground monitoring stations (e.g., from DNI measurements).

Clear-sky global irradiance: The Kasten clear sky model was modified (Ineichen et al., 2002) to exploit the new turbidity formulation and to improve its fit of observed data for very clear / high elevation locations found in the western part of the continent, while conserving its representativeness of standard temperate environments.

Ghcnew = cg1 Io cos z exp(-cg2 am (fh1 + fh2 (TL - 1))) exp(0.01*$am^{1.8}$)

With $\quad\quad\quad$ cg1 = (0.0000509 alt + 0.868)

$\quad\quad\quad\quad\quad\quad$ cg2 = 0.0000392 alt + 0.0387

Cloud-index function: The linear CI-to-GHI function was dropped in favor of a form representative of observed data. The present formulation, plotted in Fig. 4, is a fit to five environmentally distinct, very high quality ground truth stations (Albany, NY, Burlington, KS, Eugene, Gladstone and Hermiston, OR).

GHI = Ktm Ghcnew (0.0001 Ktm Ghcnew + 0.9)

With $\quad\quad\quad$ Ktm = $2.36\ CI^5 - 6.2\ CI^4 + 6.22\ CI^3 - 2.63\ CI^2 - 0.58\ CI + 1$

Differences with the simple original linear function are not very large. Nevertheless the experimental data do reveal a definite trend, with maximum departures at the upper and lower ends of the curve. At the lower end – high CI – the new function produces noticeable performance improvement for low irradiances (e.g., see fig. 6, global irradiance). At the upper end – low CI -- the curvature reflects the fact that some uncertainty exists in the exact location of the clear pixel's edge (e.g., see the lower bound points in Fig. 1).

3.3 DNI generation

DNI is obtained, as GHI, via modulation of clear-sky direct irradiance. The clear sky irradiance model was recently introduced by the authors as part of the development of the new TL formulation (Ineichen and Perez, 2002):

Bc = Min { 0.83 Io exp(- 0.09 am [TL – 1]) (0.8 + 0.196 / fh1),

$\quad\quad\quad\quad\quad\quad$ (Gcnew - Dc)/ cos Z }

where Dc is the minimum clear sky diffuse irradiance given by:

Dc = Gcnew { 0.1 [1 - 2 exp(-TL)]} {1 / [0.1+ 0.882 / fh1]}

Unlike GHI, the direct modulating factor is not derived from CI but from global, using the global-to-DNI model, DIRINT (Perez et al., 1992), in a relative mode . In this relative mode, DIRINT is used twice, once to calculate an intermediate direct

irradiance, DNI_1, from GHI and, a second time to calculate an intermediate clear sky direct irradiance, DNI_2, from Ghcnew. DNI is obtained from:

$$DNI = Bc \ [\ DNI_1 \ / \ DNI_2 \ ]$$

This approach retains the main strength of DIRINT: the use of a stability index derived from the GHI data stream (Perez et al., 1990) while it mitigates its main weakness: the lack of calibration of this model with respect to a standard clear sky profile.

3.4 Operational Model

While the modeling process has been thoroughly described above, the operation of the model on a geographic scale, either for the preparation of maps or site/time specific time series requires some degree of logistics and information processing. This logistical approach is summarized in Fig. 5. It includes several layers of gridded information. The grid size of our current archive is 0.1 degrees latitude-longitude. Ultimate achievable resolution of visible channel GOES image could approach 0.01 degree. The information gridded layers include:

Raw satellite pixels (visible channel) obtained via direct processing of primary GOES east and GOES west satellite images. We archive gridded raw pixel frames on an hourly basis.

Terrain elevation

Climatological Linke turbidity – 12 monthly layers, derived from previously gridded aerosol optical depth data (NSRDB, 1995)

Snow cover – daily gridded frames from (NOHCRS, 2002)

Specular correction factor – 216 layers (12 months by 18 hours) derived from the hourly processing of 5 years worth of raw pixel data (see sun-satellite angle effects, above).

4.   VALIDATION

4.1 Experimental Ground Truth Data

A total of ten stations, listed in Table I are used to evaluate model performance. As mentioned above data from five of these stations (*) were used to fit the CI-to-global transfer function. Most of the stations follow rigorous calibration and quality control protocols, particularly those directly or indirectly affiliated with the ARM (2002) or BSRN (2002) programs and with the Pacific Northwest network.

Albany, ARM-Burlington and FSEC are used to validate irradiances derived from GOES-East (GOES-8) data. Burns, Eugene, Gladstone, Hermiston, Klamath Falls and Kramer Junction are used for GOES-West (GOES-10). Albuquerque is used to validate irradiances derived from both satellites.

4.2 Results

The first set of validation metrics – overall observed root mean square errors (RMSE) and mean bias errors (MBE) – is presented in Table 2. We compare the old model against two versions of the new model: (1) the operational model as described in this paper, and (2) the same with monthly turbidity derived locally from the ground truth DNI measurements. The statistics are based on 96% of the points, rejecting 2% of the most extreme positive and negative differences – most of the highest differences have little to do with model intrinsic accuracy but are mostly reflective of the impact of cloud patterns on the comparison between an instantaneous measurement extended in space - the satellite pixel - and a pinpoint ground measurement extended in time - hourly integration (Zelenka et al., 1999).

The observed performance improvement is systematic for all sites using the RMSE benchmark. This is remarkable since the room for gain is not as large as the magnitude of the initial error would suggest. Because of the above-mentioned pixel-ground station discrepancy and small remaining satellite navigation uncertainties the initial is already close to achievable effective accuracy (Zelenka et al., 1999). As it is, the new model approaches this limit for GHI at several of the sites. Inspection of the MBE benchmark also reveals overall improvement – Note in particular that the strongest underestimations (Albuquerque, Kramer) and overestimations (Gladstone) have been reduced. The model using local measurement-based turbidity shows only slight additional improvement. The case of Florida stands out, with a much stronger initial RMSE and MBE and small accuracy improvement. The causes for this will have to be investigated further. At present the two major suspected causes are (1) the humid subtropical climate with frequent broken cloud patterns, and more likely, (2) the fact Cocoa is situated at the edge of a body of water, with a satellite pixel straddling two very different minimum brightness environments.

Model performance improvement may be qualitatively visualized in Figs. 6 and 7 that compare the old and the new (with generic TL) performance in Albuquerque, NM for GOES west. Note that Albuquerque provides a fully independent model test bed as this site was not used to fit the CI-to-GHI index function. The reduction of scatter and high-end bias is particularly striking for DNI. Much of the improvement at that site stems from the utilization of the pixel specific look-up table describing the local sun-satellite angle effect. In the old model, enhanced brightness of the ground peaking in early afternoon is mistaken as increased cloud index resulting in a severe DNI underestimation. Much of this shortcoming is corrected with the new model.

Overall bias may appear reasonable only to hide seasonal effects that may cancel-out. So, another gauge of model performance improvement is to observe the variations of seasonal biases. Fig. 8 compares the seasonal DNI bias traces for all sites. The new model traces are noticeably more compact showing more site-to-site as well as season-to-season consistency.

5. CONCLUSION

We have presented a new simple model capable of exploiting geostationary satellite visible images for the production of site/time specific global and direct irradiances. The model exhibits systematic performance improvement for all tested locations representing a wide range of climatic environments. As it is, the level of observed RMSE at some of the test stations approaches the effective accuracy limit previously discussed by the authors and colleagues (Zelenka et al., 1999). The new model is particularly efficient at correcting possible distortions resulting from certain types of ground surfaces.

Future work will focus on (1) addressing remaining ground specularity effects that may leave a trace in the production of microclimatic solar resource maps; (2) investigating other climates, particularly subtropical and tropical, which have only been marginally covered here; (3) investigating whether additional satellite channels (in particular IR) may lead any noticeable cloud index detection and model performance improvement; (4) comparing this model with other models (e.g., Broesamle et al., 2001) using common ground truth stations as will been done as part of the SWERA program (SWERA, 2002).

6. ACKNOWLEDGMENTS

7. REFERENCE

ARM (2002): Atmospheric Radiation Measurement Program, http://www.arm.gov/

Broesamle, H., H. Mannstein, C. Schillings and F. Trieb, (2001): Assessment of Solar Electricity Potentials in North Africa Based on Satellite Data and a Geographic Information System. Solar Energy 70, pp. 1-12

BSRN (2002): Baseline Surface Radiation Network, http://bsrn.ethz.ch/

Cano, D., J.M. Monget, M. Aubuisson, H. Guillard, N. Regas and L. Wald, (1986): A Method for the Determination of Global Solar Radiation from Meteorological Satellite Data. Solar Energy 37, pp. 31-39

Ineichen, P. and R. Perez, (1999): Derivation of Cloud Index from Geostationary Satellites and Application to the Production of Solar Irradiance and Daylight Illuminance Data Theoretical and Applied Climatology Vol. 64, 119-130.

Ineichen, P., R. Perez, M. Kmiecik and D. Renné, (2000), Modeling Direct Irradiance from GOES Visible Channel Using Generalized Cloud Indices. Proc. 10th Conference on Satellite Meteorology and Oceanography, Long Beach, CA, pp. 133-136. American Meteorological Society, Boston, MA.

Ineichen, P. and R. Perez, (2002): A new airmass independent formulation for the Linke turbidity coefficient. Solar Energy Vol. 73, 3 pp. 151-157

Kasten F. (1980): A simple parameterization of two pyrheliometric formulae for determining the Linke turbidity factor. Meteorol. Rdsch. 33, 124-127

Kasten, F., (1984): Parametriesirung der Globalstahlung durch Bedeckungsgrad und Trubungsfaktor. Annalen der Meteorologie Neue Folge, 20, pp. 49-50

Noia M., C. Ratto, and R. Festa, (1993): Solar irradiance estimation from geostationary satellite data: I. Statistical models, II. Physical models. Solar Energy 51, 449-465.

NOHRSC, (2002): National Operational Hydrologic Remote Sensing Center. http://www.nohrsc.nws.gov/

NSRDB, (1995): National Solar Radiation Data Base - Final Technical Report, Volume 2, 1995. NREL/TP-463-5784

Perez, R., P. Ineichen, R. Seals and A. Zelenka, (1990): Making Full Use of the Clearness Index for Parameterizing Hourly Insolation Conditions. Solar Energy 45, pp. 111-114

Perez, R., P. Ineichen, E. Maxwell, R. Seals and A. Zelenka, (1992): Dynamic Global-to-Direct Irradiance Conversion Models. ASHRAE Transactions-Research Series, pp. 354-369

Perez, R., R. Aguiar, M. Collares-Pereira, D. Dumortier, V. Estrada-Cajigal, C. Gueymard, P. Ineichen, P. Littlefair, H. Lund, J. Michalsky, J. A. Olseth, D. Renné, M. Rymes, A. Skartveit, F. Vignola, A. Zelenka, (2001): Solar Resource Assessment – A Review. Solar Energy-The State of the Art, Chapter 10, section 10.4.4 (Zelenka), James & James, London

Pinker, R. T., R. Frouin, and Z. Li, (1995): A review of satellite methods to derive surface shortwave irradiance. Remote Sens. Environ. 51, 108-124.

Pinty, B. and M. M. Verstraete, (1991): Extracting Information on Surface Properties from Bidirectional Reflectance Measurements. J Geophys. Res. 96, 2865-2874

Schmetz, J. (1989): Towards a Surface Radiation Climatology: Retrieval of Downward Irradiances from Satellites. Atmos Res., 23, pp. 287-321

SWERA (2002): Solar and Wind Resource Assessment, http://www.uneptie.org/energy/act/re/fs/swera.pdf

Unidata (2002): Unidata Internet Data Distribution System. http://my.unidata.ucar.edu/

Zelenka, A., Perez R, Seals R. and Renné D., (1999): Effective Accuracy of Satellite-derived irradiance, Theoretical and Applied Climatology, 62, 199-207

Figure Captions

Figure 1: Satellite Dynamic Range – GOES-8 southeastern US, 1997-2000. Note the lower bound seasonal variation and the upper bound decrease from satellite calibration decay.

Figure 2: Impact of snow on the dynamic range's lower bound in Burns, OR, January-May 1999. In the absence of external information on snow cover, the dotted line would be used as the dynamic range's lower bound by the model, resulting in marked underestimation. The snow events force the lower bound to re-initialize based upon the value of incoming pixels, resulting in the black lower bound trace.

Figure 3: Impact of ground specular reflectivity on lower bound in Albuquerque -- GOES-West data. The PM trace is well above the AM trace because the arid ground appears considerably brighter when the sun satellite reaches a minimum in the afternoon. The original model would infer the lower bound from all the points (original trace), leading to irradiance underestimation in the afternoon as clear pixels would be interpreted as having significant cloud indices.

Figure 4: Illustration of the new CI-to-GHI function fitted to all available data. The dotted line illustrates the linear function of the original model. The largest departure is observed for high cloud indices, showing that the original model tended to underestimate irradiance for high pixel brightness. A small difference is also noticeable for very low indices, showing that the original model tended to underestimate irradiance -- this small underestimation tendency was compounded when extracting direct irradiance from global.

Figure 5: This figure illustrates all the geographically gridded data sets that are used operationally in the North-American model, including hourly or _ hourly image pixels, terrain elevation, monthly Linke turbidity, daily snow-cover updates and the ground specular reflectivity correction factors (monthly-hourly averages).

Figure 6: Modeled vs. measured hourly global irradiance for the old and new model in Albuquerque using GOES-West as model input. Model performance improvement at the high end results from taking specular ground reflectivity into account. Improvement at the low end, results from a better CI fit (see Fig. 3)

Figure 7: Comparing, measured and modeled typical clear-sky DNI daily profiles in Albuquerque, NM. The original model's deficit peaks in mid afternoon when the local sun-satellite angle reaches its minimum value.

Figure 8: Comparing old and new model Mean Bias Error monthly trends for direct irradiance for all stations.

Table Titles

Table 1:   Ground Truth Stations

Table 2:   Model RMSE and MBE for global and Direct Irradiance
[note, the new column corresponds to climatological turbidity, wile new* corresponds to local measurements-derived turbidity]
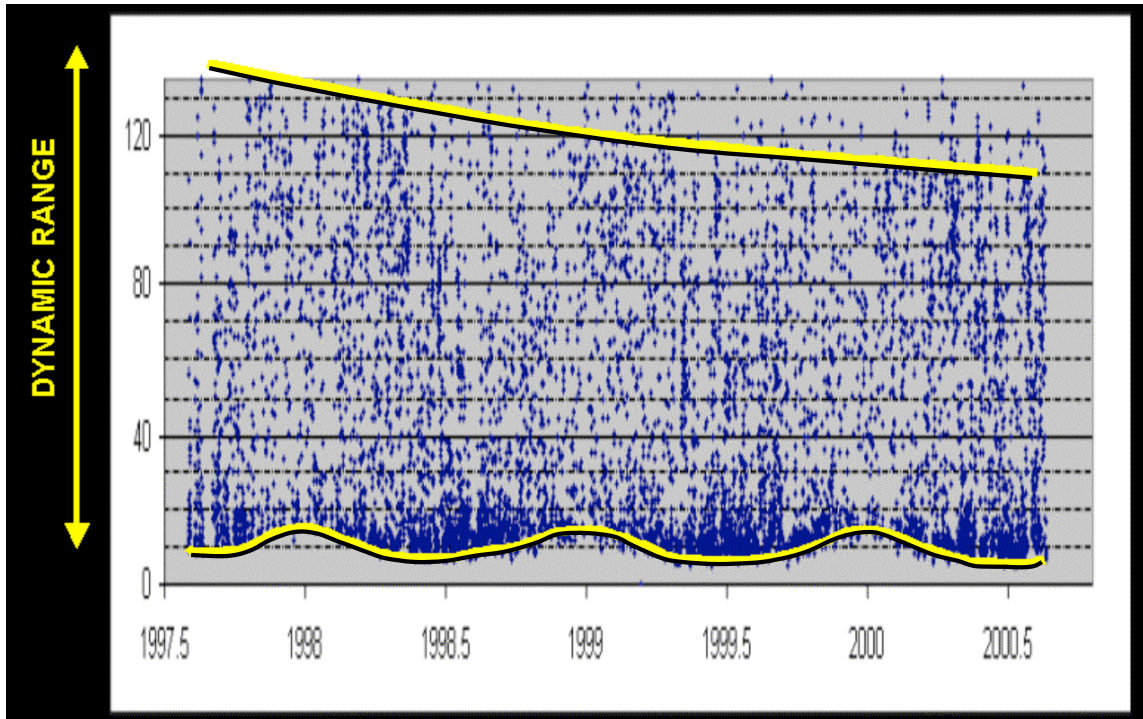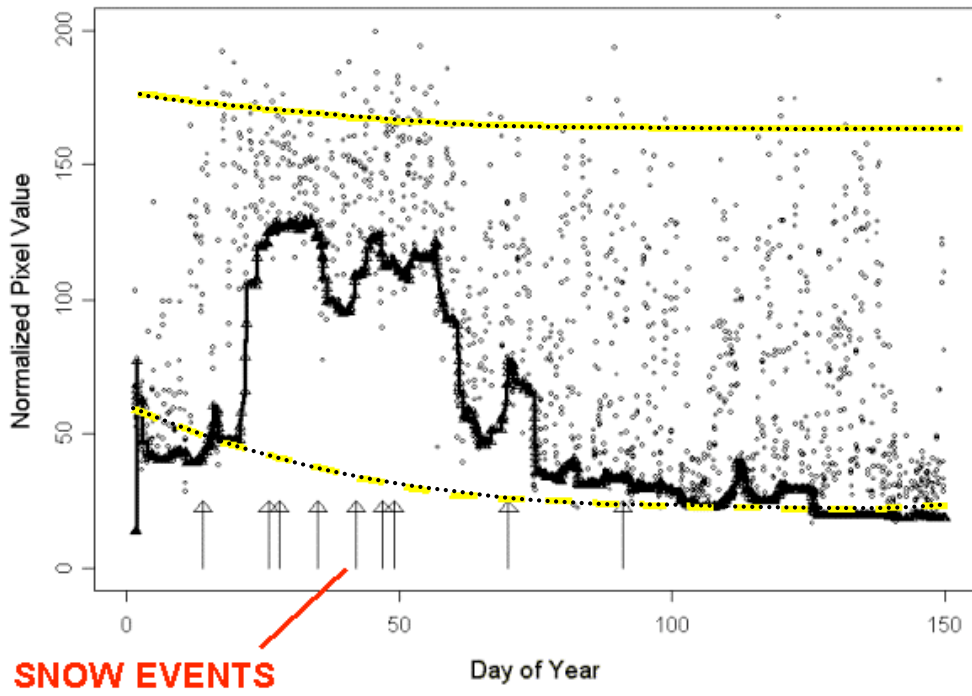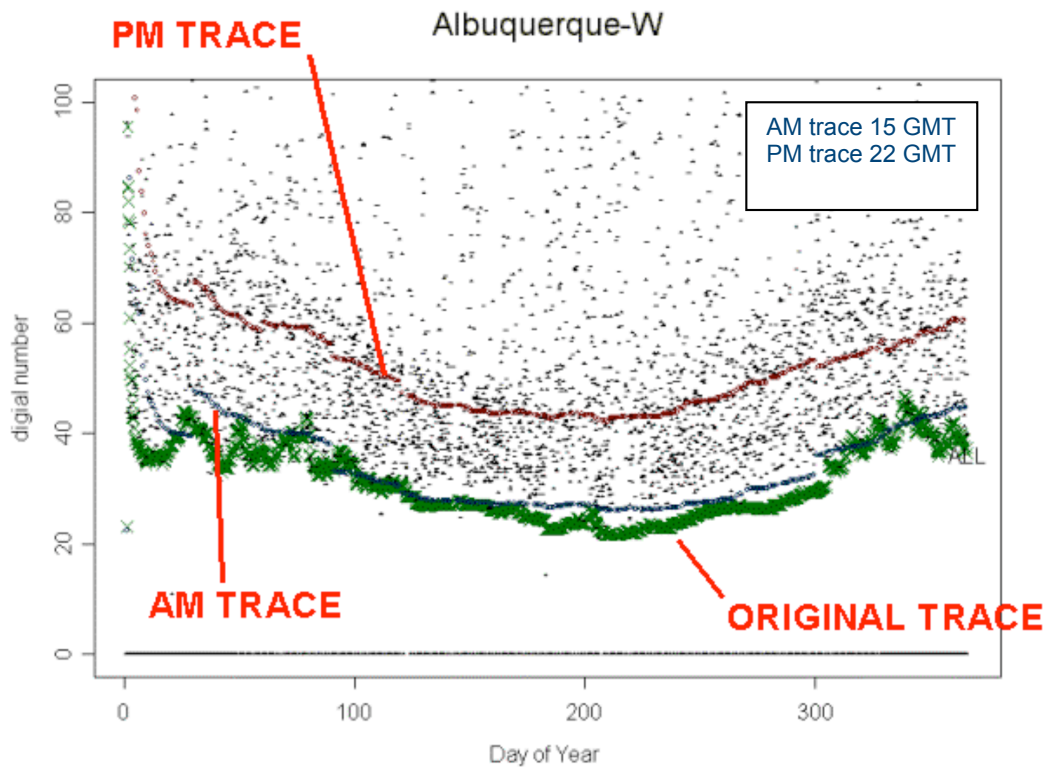
Figure 1

Figure 2

SNOW EVENTS

Figure 3

Albuquerque-W

Figure 4

Figure 5

Pixels hourly

Terrain elevation

Turbidity (12 months)

Snow cover (daily)

Specular correction
(monthXhour)
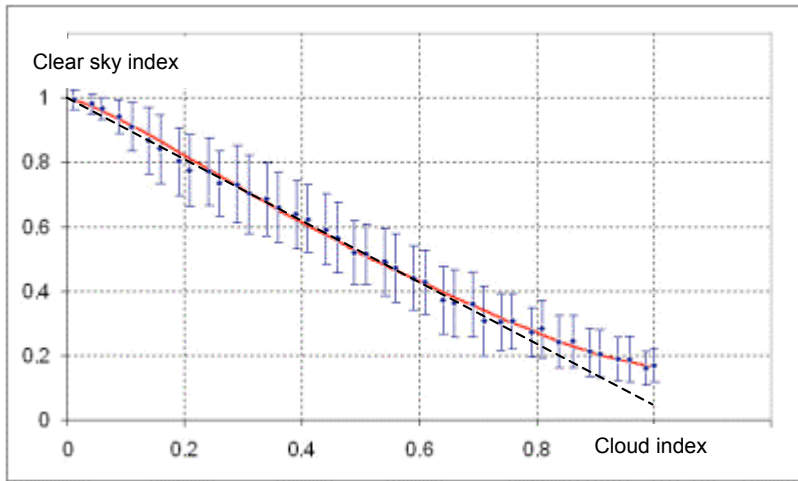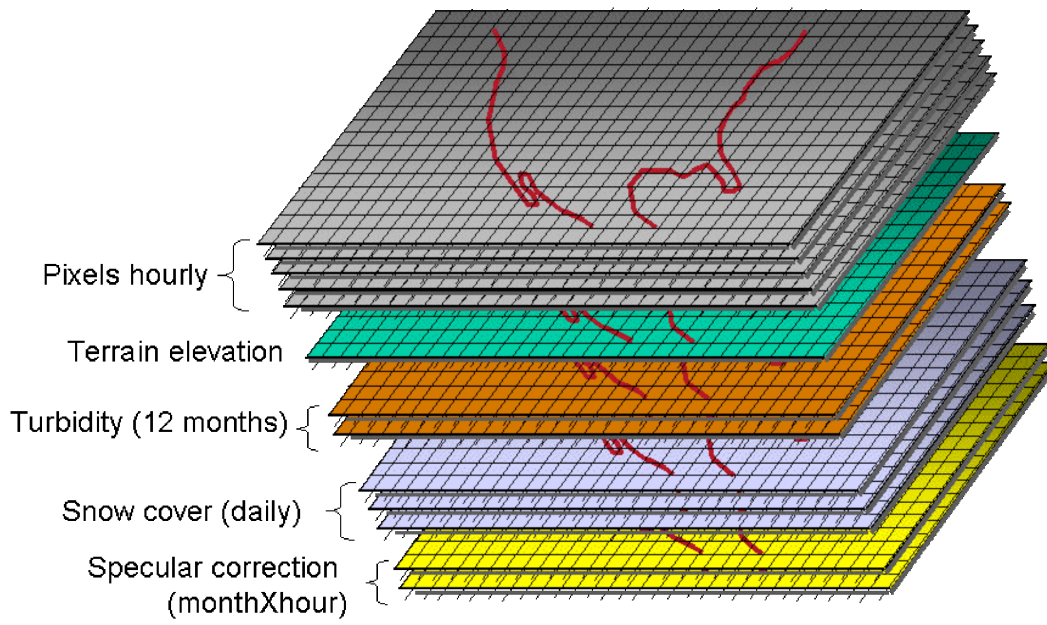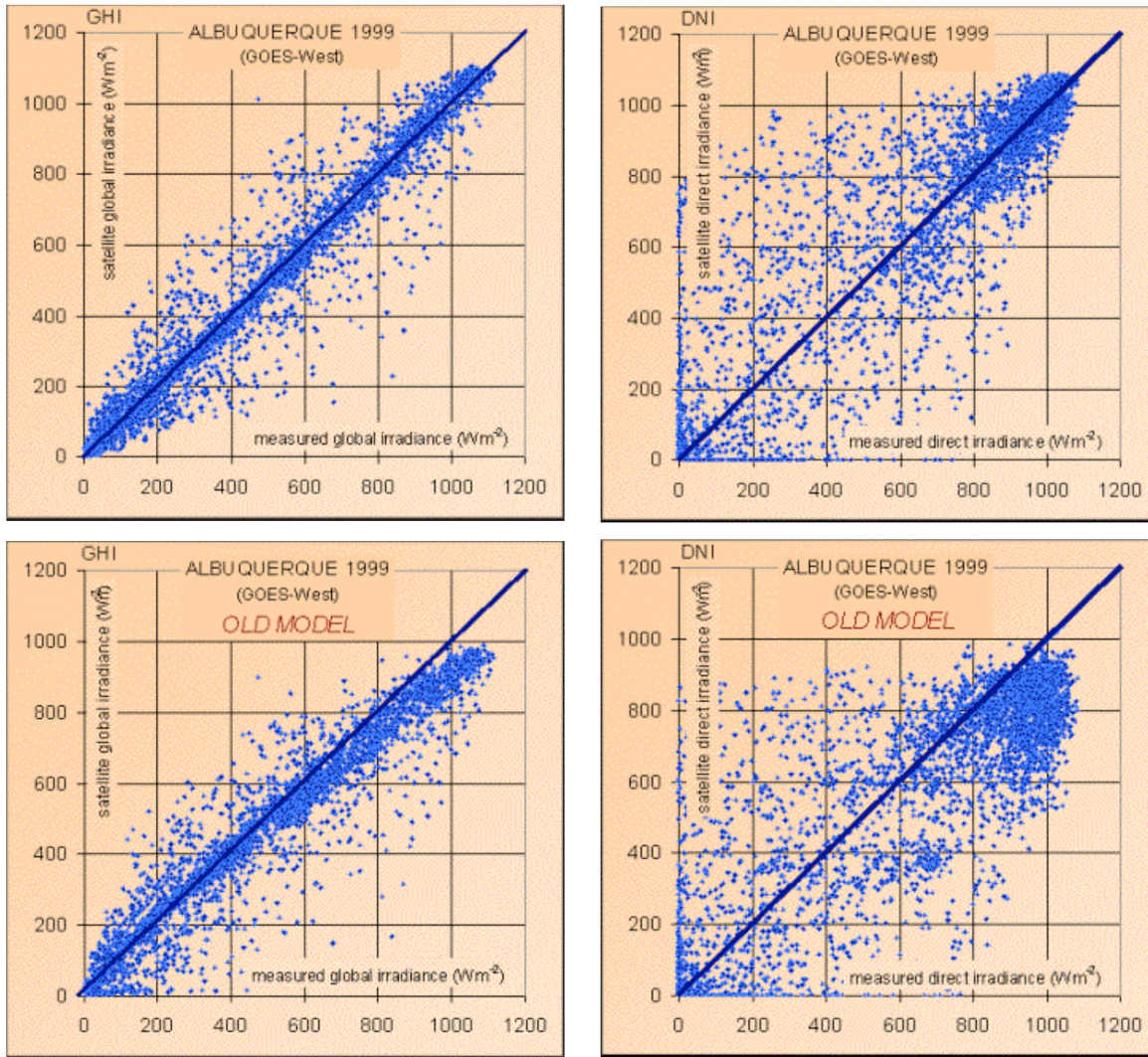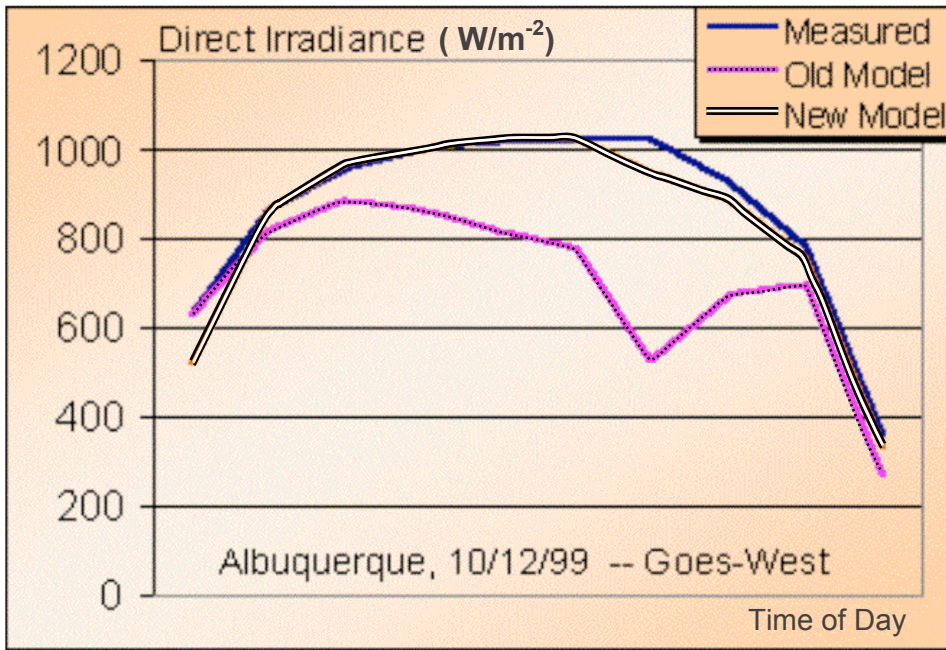
Figure 6

Figure 7

Figure 8
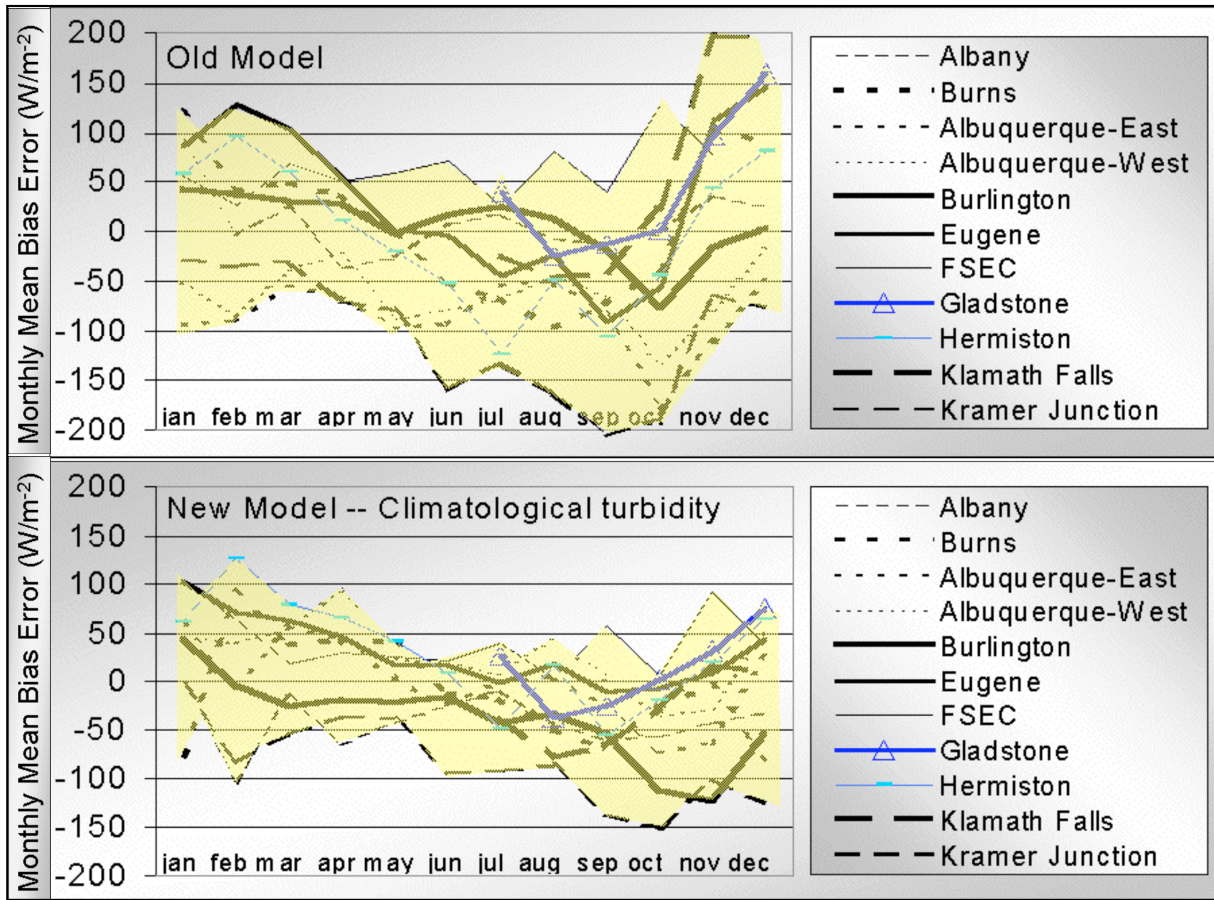
Table 1

Site	Climate	Lat (°)	Long (°)	Notes
Albany, NY (1999)	Humid continental	42.7	-73.8	BSRN [ref]
Burns, OR (1999-2000)	Semi-arid, high elev.	43.6	-119.1	Pacific Northwest network
Albuquerque, NM (1999)	Arid, high elevation	35.1	-106.6	Sandia Natl. Labs, ARM protocol
ARM-Burlington, KS (1999)	Dry continental	38.1	-95.7	ARM –SGP extended facility [ref]
Eugene, OR (1999)	Temperate	44.0	-123.1	Pacific Northwest network
FSEC-Cocoa, FL (1999)	Subtropical	28.3	-80.7	Florida Solar Energy center
Gladstone, OR, (part-1999)	Temperate, humid	45.3	-122.6	Pacific Northwest network
Hermiston, OR (1999-2000)	Temperate, dry	45.8	-119.3	Pacific Northwest network
Klamath Falls, OR (pt-1999)	Temperate dry	42.2	-121.8	Pacific Northwest network
Kramer Junction, CA (1999)	Arid	35.0	-117.5	SEGS power plant monitoring

Table 2

GLOBAL		RMSE			MBE		
Day-time avg - Wm-2		old	new	new*	old	new	new*
Albany	326	72	68	69	-7	-11	-1
Burns-99	391	89	79	79	-20	-21	-20
Burns-00	383	69	62	62	2	1	2
Albuq. (Goes-E)	485	76	69	69	-31	-3	-5
Albuq. (Goes-W)	486	90	80	80	-22	1	-1
ARM-Burlington	355	57	51	51	6	-1	2
Eugene	311	64	53	53	3	7	4
FSEC-Cocoa	421	121	115	118	34	31	52
Gladstone	290	64	60	60	18	17	24
Hermiston-99	358	52	45	45	-6	2	-2
Hermiston-00	357	47	44	44	7	15	11
Klamath-Falls	357	58	47	50	18	7	16
Kramer Junction	487	69	48	49	-19	-11	8
All sites	385	61	54	54	-4	0	3

DIRECT		RMSE			MBE		
Day-time avg - Wm-2		old	new	new*	old	new	new*
Albany	345	165	154	155	5	-40	-3
Burns-99	483	204	190	188	-33	-41	-35
Burns-00	477	198	172	171	-1	-5	0
Albuq. (Goes-E)	629	179	169	165	-84	-4	-19
Albuq. (Goes-W)	629	205	187	185	-64	26	8
ARM-Burlington	397	131	121	117	5	-42	-28
Eugene	305	158	116	112	18	23	7
FSEC-Cocoa	339	209	193	207	62	36	100
Gladstone	276	151	118	122	38	11	48
Hermiston-99	494	151	133	129	-19	21	2
Hermiston-00	434	163	138	135	-17	25	5
Klamath-Falls	493	199	163	174	33	-17	31
Kramer Junction	672	231	156	161	-104	-83	27
All sites		161	137	137	-19	-11	4